Available online at www.sciencedirect.com
SCIENCE DIRECT®
Experimental Thermal and Fluid Science 27 (2003) 525–535
Experimental Thermal and Fluid Science
www.elsevier.com/locate/etfs

Strong interactions between free-surface aeration and turbulence in an open channel flow

Hubert Chanson *, Luke Toombes

Department of Civil Engineering, University of Queensland, Brisbane, Qld 4072, Australia

Received 31 March 2002; accepted 30 June 2002

Abstract

High-velocity free-surface flows may be characterised by strong free-surface aeration. In turn the entrained air bubbles are expected to interact with the flow turbulence. An experimental study was conducted in supercritical open channel flows down a cascade. Measurements included time-averaged air–water flow properties, air and water chord sizes, and interfacial areas. High levels of turbulence were associated consistently with large air–water interfacial areas. Altogether the study contributes to a better understanding of the basic interfacial processes in re-aeration cascades.

Keywords: Free-surface aeration; Turbulence; Experiments; Interfacial properties; Open channel flow; Staircase chute

1. Introduction

Staircase channels have been used in a variety of applications in civil and environmental engineering applications [3]. These include dam spillways, storm waterways, staircase fountains and re-oxygenation cascades (Fig. 1). Stepped chute flows are often characterised by strong air–water mixing. Fig. 1A shows white waters in a stepped river training system. Fig. 1B illustrates free-surface aeration in a re-aeration cascade along the Calumet water way near Chicago. In operation, the dissolved oxygen aeration efficiency of the structure, corrected to a temperature of 15 °C, is nearly 95% [16].

On stepped chutes, the air–water mass transfer of chemicals is enhanced by the aeration of the flow, strong turbulent mixing and significant residence time. The large amount of entrained air bubbles increases the air–water interface area due to the cumulative bubble surface area. For example, if the mean bubble diameter is 1 mm and the air content is 15%, the specific interface area is 900 m^2 per cubic metre of air and water. The mass transfer rate of a chemical across an interface varies directly as the coefficient of molecular diffusion, the negative gradient of gas concentration and the interface area. If the chemical of interest is volatile (e.g. oxygen), the transfer is controlled by the liquid phase and the gas transfer of the dissolved chemical may be expressed as

$$\frac{\partial}{\partial t} C_{gas} = k_L * a * (C_{sat} - C_{gas}) \quad (1)$$

where k_L is the liquid film coefficient, a is the specific surface area, C_{gas} is the local dissolved gas concentration and C_{sat} is the concentration of dissolved gas in water at equilibrium [8]. Many studies have assumed implicitly that the term $(k_L * a)$ is a constant (e.g. [12,13]). The assumption is incorrect. Detailed studies showed that the mass transfer coefficient, k_L, in turbulent gas–liquid flows is almost constant regardless of bubble sizes and flow situations.(e.g. [11]). But the interface area varies greatly along a channel as a function of the air entrainment rate, flow turbulence and interactions between entrained bubbles and turbulence. Toombes and Chanson [5,21] showed that the integration of the mass transfer equation (Eq. (1)), based upon measured air–water interface area, may provide a genuine, accurate estimate of aeration performances. However it is yet impossible to predict the air–water surface area because of the dual interactions between interfacial properties and turbulence characteristics.

* Corresponding author. Tel.: +61-7-3365-3516; fax: +61-7-3365-4599.
E-mail address: h.chanson@mailbox.uq.edu.au (H. Chanson).

0894-1777/03/$ - see front matter © 2003 Elsevier Science Inc. All rights reserved.
doi:10.1016/S0894-1777(02)00266-2

Nomenclature

a	air–water specific area (1/m), defined as the interfacial surface area per unit volume of air and water
a_{mean}	depth-averaged specific interface area (1/m): $a_{mean} = \frac{\Lambda}{Y_{90}} * \int_{y=0}^{y=Y_{90}} a * dy$
C	void fraction defined as the volume of air per unit volume, also called air concentration
C_{gas}	concentration of dissolved gas in water (kg/m^3)
C_{sat}	gas saturation concentration in water (kg/m^3)
D_o	dimensionless coefficient
d	characteristic depth (m) defined as $d = \int_0^{Y_{90}} (1-C) * dy$ and measured normal to the channel slope at the edge of a step
d_{ab}	air bubble size (m)
d_c	critical flow depth (m); for a rectangular channel: $d_c = \sqrt[3]{q_w^2/g}$
F	bubble count rate (Hz), i.e., number of bubbles detected by the probe sensor per second
Fr	Froude number
g	gravity constant (m/s^2) or acceleration of gravity; $g = 9.80$ m/s^2 in Brisbane
h	height of steps (m) (measured vertically)
K'	integration constant
k_L	liquid film coefficient (m/s)
k_s'	equivalent sand roughness height (m)
Mo	Morton number
q	discharge per unit width (m^2/s)
Re	Reynolds number
Tu	turbulence intensity defined as Tu $= u'/V$
t	time (s)
u'	root mean square of longitudinal component of turbulent velocity (m/s)
V	velocity (m/s)
V_c	critical velocity (m/s); for a rectangular channel: $V_c = \sqrt[3]{g * q_w}$
V_{90}	characteristic velocity (m/s) where the air concentration is 90%
v'	root mean square of lateral component of turbulent velocity (m/s)
W	channel width (m)
w	water flow
x	longitudinal distance (m)
Y_{90}	characteristic depth (m) where the air concentration is 90%
y	distance (m) from the pseudo-bottom (formed by the step edges) measured perpendicular to the flow direction

Greek symbols

α	channel slope
λ	dimensionless coefficient
μ	dynamic viscosity (N s/m^2)
ρ	density (kg/m^3)
σ	surface tension between air and water (N/m)

Other symbol

$\varnothing$	diameter (m)

Subscripts

air	air flow
c	critical flow conditions

It is the aim of this work to describe accurately air bubble entrainment in turbulent free-surface flows, and to present new evidence contributing to a better understanding of the multiphase flow dynamics. The study investigates free-surface flows down a stepped cascade (Figs. 1–3). The structure of the air–water flows is described, and a new analysis of the interfacial properties is presented.

2. Similitude and physical modelling

In a staircase channel of a given geometry, small discharges behave as a succession of free-falling nappes called nappe flow regime [3,15]. With increasing flow rates, a transition flow regime takes place. A dominant flow feature is the chaotic appearance with spray, splashing and irregular droplet ejections. At larger discharges, the flow skims over the step edges as illustrated in Fig. 3 (skimming flow regime). Cavity recirculation is very energetic and flow resistance is primarily step form drag. Free-surface aeration is very intense, and its effects cannot be neglected.

Analytical and numerical studies of free-surface aeration in stepped chute flows are complex because of the large number of relevant equations. Experimental investigations are often preferred and this study is no exception.

2.1. Dimensional analysis

Laboratory studies of air–water flows require the selection of an adequate similitude. In a channel made of flat horizontal steps, a complete dimensional analysis yields

$$F\left(C; \frac{V}{\sqrt{g*d}}; \frac{u'}{V}; \frac{v'}{V}; \frac{d_{ab}}{d}; \frac{x}{d}; \frac{y}{d}; \rho_w * \frac{q_w}{\mu_w}; \frac{g*\mu_w^4}{\rho_w*\sigma^3}; \times \frac{q_w}{\sqrt{g*h^3}}; \frac{W}{h}; \alpha; \frac{k_s'}{h}\right) = 0 \quad (2)$$

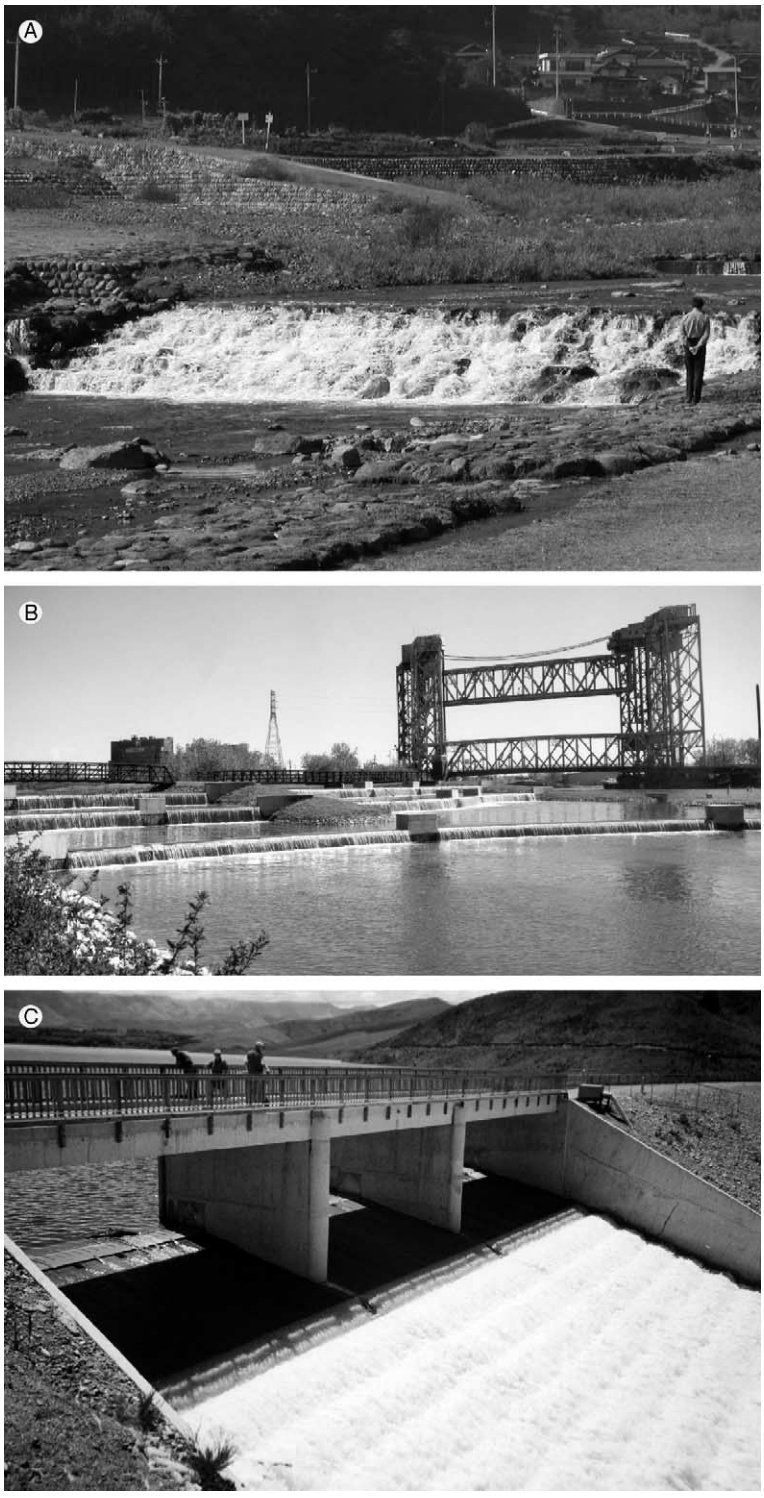

Fig. 1. Examples of free-surface aeration in staircase chute flows: (A) stepped sabo works on Oyana-gawa (Japan) on 1 November 2001; (B) re-oxygenation cascade in Chicago (Courtesy of the Metropolitan Water Reclamation District of Greater Chicago)—Sidestream Elevated Pool Aeration (SEPA) station along the Calumet waterway; (C) Opuha dam stepped spillway in operation (Courtesy of Tonkin and Taylor).

where C is the void fraction, V is the velocity, d is the equivalent clear-water depth, g is the gravity acceleration, u' is the root mean square of the axial component of turbulent velocity, v' is the root mean square of lateral component of turbulent velocity, d_{ab} is a characteristic bubble size, x is the coordinate in the flow direction, y is the distance measured normal to the pseudo-bottom formed by the step edges (Fig. 2), q_w is the water discharge per unit width, μ_w and ρ_w the dynamic viscosity and density of water respectively and σ the surface tension,

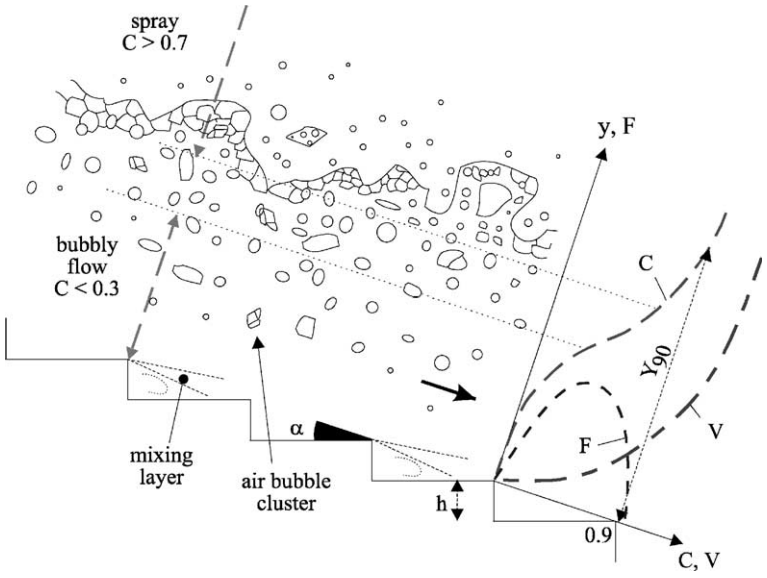

Fig. 2. Air–water flow: definition sketch.

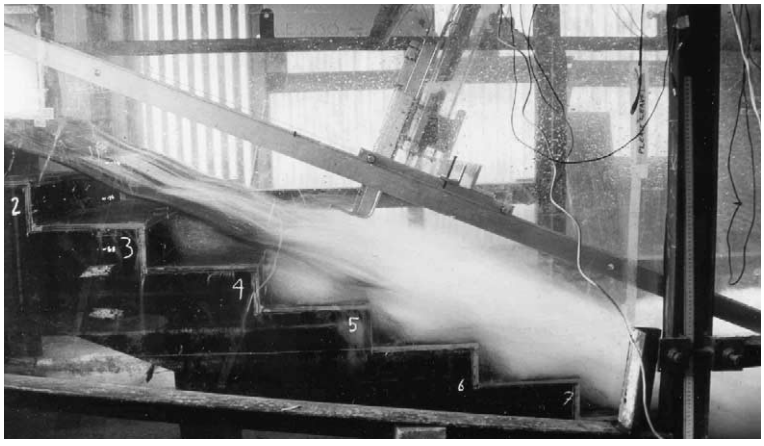

Fig. 3. Experimental flow conditions: skimming flow ($q_w = 0.114$ m^2/s, $h = 0.1$ m, $l = 0.25$ m); flow from the left to the right; note the inception of free-surface aeration downstream of the step edge 4, and the probe travelling mechanism.

h is the step height, W the channel width, α is the angle between the horizontal and the pseudo-bottom formed by the step edges (Fig. 2), and k_s' is the skin roughness height. For air–water flows, the equivalent clear water depth d is defined as

$$d = \int_{y=0}^{y=Y_{90}} (1 - C)^* \mathrm{d}y \tag{3}$$

where Y_{90} is the characteristic distance were $C = 0.9$. In Eq. (2), the first four terms (i.e. C, $V/\sqrt{g * d}$, u'/V, d_{ab}/d) are dimensionless characteristics of the air–water flow field at a location $\{x/d, y/d\}$. The seventh and eighth terms are Reynolds and Morton numbers respectively. The last three terms characterise the cavity shape and the skin friction effects on the cavity walls.

In free-surface flows, gravity effects are important and most laboratory studies, including the present study, must be based upon a Froude similitude (e.g. [2,10]). The scaling of free-surface aeration implies first that the air entrainment rate q_{air}/q_w must be identical in model and prototype, where q_{air} is the entrained air flux. Second the entrapment of air bubbles and the mechanisms of air bubble breakup and coalescence are dominated by surface tension. Their scaling must be based upon a Weber similitude. Flow resistance in stepped channels is predominantly form drag associated with viscous and turbulent dissipation in the step cavity [7,15]. Dynamic similarity implies a Reynolds similitude.

For geometrically similar models, it is impossible to satisfy simultaneously more than one similitude, and scale effects will exist when one or more Π-terms have different values between model and prototype. For example, in small size models based upon a Froude si-

militude, the air entrainment process may be affected by significant scale effects (e.g. [1,22]).

2.1.1. Discussion

For a stepped chute study based upon a Froude similitude, scale effects in terms of flow resistance are small when the Reynolds number and step height satisfy: $\rho_w * q_w/\mu_w > 2.5\ E+4$ and $h > 0.02$ m [7]. In terms of free-surface aeration, Wood [22] and Chanson [1] recommended that the ratio of prototype to model dimensions be less than 10–15.

In the present study, detailed air–water measurements were conducted in a large-size facility. The chute geometry and flow conditions satisfied: $h = 0.1$ m, $\rho_w * q_w/\mu_w = 3\ E+4$ to $2.6\ E+5$, $g * \mu_w^4/(\rho_w * \sigma^3) = 1.1\ E-6$, and $Fr = 3.9$ to 6. The large size of the facility ensures that the experimental results may be up-scaled with negligible scale effects for geometric scaling ratios up to 10:1. For example, present laboratory conditions corresponded to 3:1, 10:1 and 6:1 scale models of the prototype conditions shown in Figs. 1A, B and C respectively. Further two flow regimes (transition and skimming) were investigated, providing a broad spectrum of flow conditions.

For completeness, Eq. (2) does not include a Weber number term. Indeed, any combination of the Froude, Reynolds and Weber numbers is dimensionless and may be used to replace one of them. In the above analysis, the Weber number is replaced by the Morton number $Mo = (g * \mu_w^4)/(\rho_w * \sigma^3)$, also called liquid parameter:

$$Mo = \frac{We^3}{Fr^2 * Re^4} \tag{4}$$

2.2. Experimental setup

Experiments were conducted at the University of Queensland in a 1-m wide channel (Fig. 3). The test section consisted of a broad-crest followed by nine identical steps ($h = 0.1$ m) made of marine ply. Two chute slopes were investigated: $\alpha = 15.9°$ and $21.8°$ ($l = 0.35$ and 0.25 m respectively). The flow rate was supplied by a pump controlled with an adjustable frequency ac motor drive, enabling an accurate discharge adjustment in a closed-circuit system. The discharge was measured from the upstream head above crest with an accuracy of about 2%. Air–water flow properties were measured using a double-tip probe ($\varnothing = 0.025$ mm for each sensor). The probe sensors were aligned in the flow direction and excited by an air bubble detector (AS25240). The probe signal was scanned at 20 kHz per sensor for 20 s. The translation of the probe in the direction normal to the channel invert was controlled by a fine adjustment travelling mechanism connected to a Mitutoyo™ digimatic scale unit. The error on the vertical position of the probe was less than 0.1 mm. Flow visualisations were conducted with a digital video-camera and high-speed still photographs (Fig. 3).

Experimental investigations were conducted for flow rates ranging from 0.046 to 0.182 m^3/s although the focus was on the highly aerated transition and skimming flows. Measurements were conducted at the outer step edges. Note that uniform equilibrium flow conditions were not achieved at the downstream end of the chute because the flume was relatively short.

3. Advective diffusion of air bubbles

At the upstream end of the cascade, the flow is smooth and no air entrainment occurs. After a few steps the flow is characterised by a strong air entrainment (Fig. 3). Downstream, the two-phase flow behaves as a homogeneous mixture[1]. The exact location of the interface becomes undetermined, and there are continuous exchanges of air–water and of momentum between water and atmosphere. The air–water mix consists of water surrounding air bubbles (bubbly flow, $C < 30\%$), air surrounding water droplets (spray, $C > 70\%$) and an intermediate flow structure for $0.3 < C < 0.7$ (Fig. 2). Waves and wavelets may propagate along the free-surface [20].

The advective diffusion of air bubbles may be described by analytical models. In transition flows, the distributions of void fraction follow an exponential profile:

$$C = K' * \left(1 - \exp\left(-\lambda * \frac{y}{Y_{90}}\right)\right) \tag{5}$$

where y is distance measured normal to the pseudo-invert, Y_{90} is the characteristic distance where $C = 90\%$, K' and λ are dimensionless functions of the mean air content only. Eq. (5) compares favourably with the data (Fig. 4 Top) but for the first step edge downstream of the inception point of free-surface aeration and for the deflecting jet flow. In skimming flows, the air concentration profiles follow a hyperbolic tangent function:

$$C = 1 - \tanh^2\left(K' - \frac{\frac{y}{Y_{90}}}{2D_o} + \frac{\left(\frac{y}{Y_{90}} - \frac{1}{3}\right)^3}{3 * D_o}\right) \tag{6}$$

where K' is an integration constant and D_o is a function of the mean void fraction only. Data are compared successfully with Eq. (6) (Fig. 4 Bottom). Although Fig. 4 highlights different shapes of void fraction distribution between transition and skimming flows, Eqs. (5) and (6) are theoretical solutions of the same advection diffusion equation for air bubbles, assuming different air bubble diffusivity profiles [6]. Toda and Inoue [19] obtained a similar result based upon numerical modelling using both Lagrangian and Eulerian approaches.

Fig. 5 presents dimensionless distributions of bubble count rates $F^* d_c/V_c$, where d_c is the critical depth and

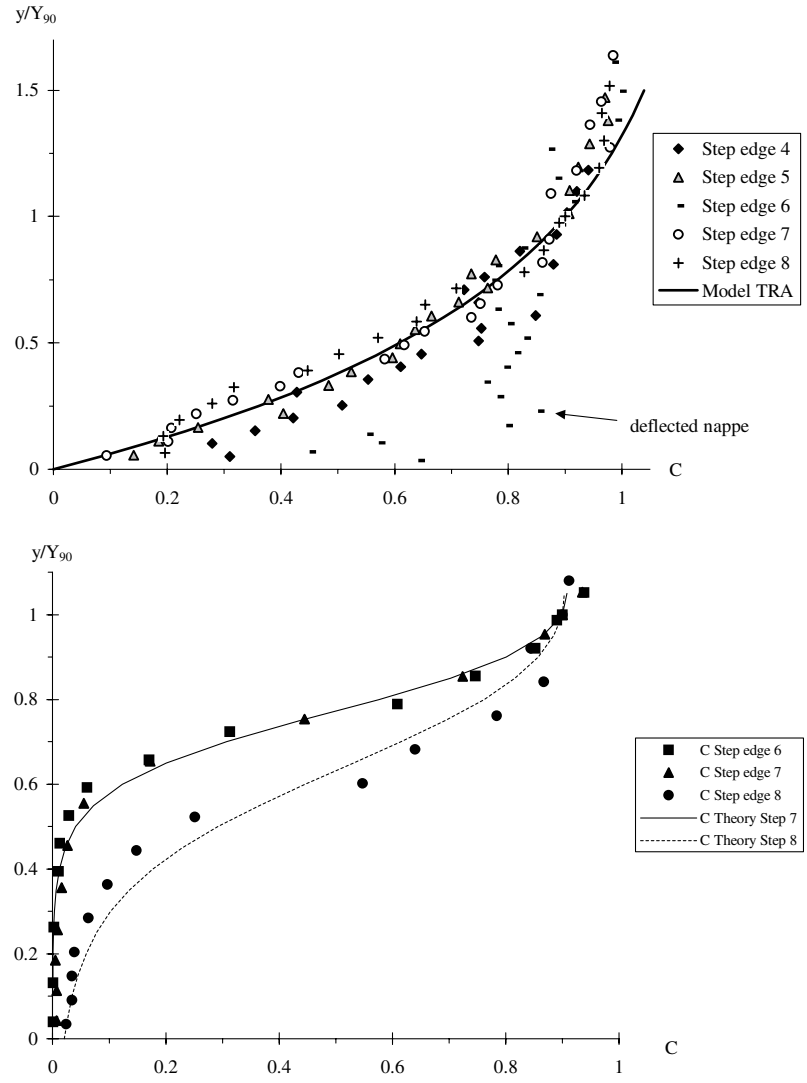

Fig. 4. Dimensionless distributions of void fraction in stepped chute flow ($\alpha = 21.8°$, $h = 0.1$ m) (data measured at outer step edges). Top: transition flow, $q_w = 0.058$ m^2/s. Bottom: skimming flow: $q_w = 0.182$ m^2/s.

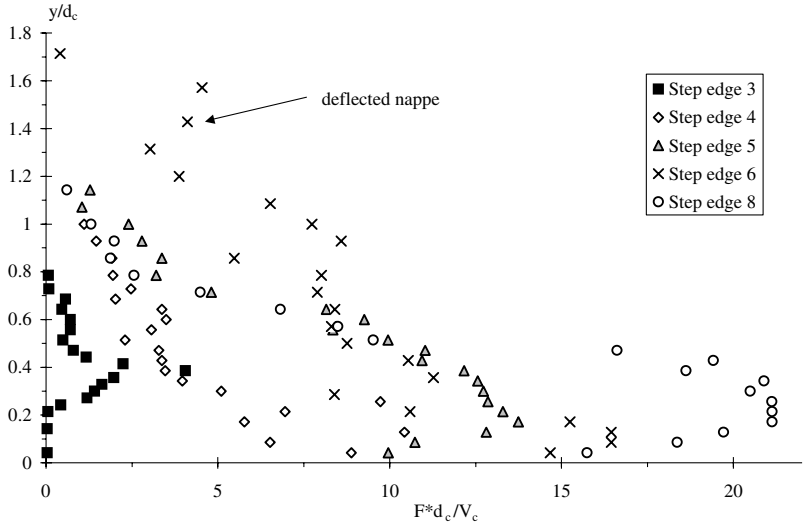

Fig. 5. Dimensionless bubble count rate distributions ($h = 0.1$ m, $l = 0.25$ m); transition flow, $q_w = 0.058$ m^2/s.

V_c is the critical flow velocity. For rectangular channels, $d_c = \sqrt[3]{q_w^2/g}$ and $V_c = \sqrt{g * d_c}$. For that flow rate, the data show maximum bubble count rates of about 163 and 250 bubbles per second at step edges 5 and 8 respectively and the maxima were always observed for $C \approx 50\%$. Further, the relationship between bubble count rate and void fraction was unique as demonstrated by Toombes [20]. Toombes proposed a model comparing favourably with experimental data obtained in water jets discharging into air, smooth-chute flows and stepped chute flows.

4. Interfacial properties

4.1. Bubble/droplet chord sizes

Air and water chord lengths were measured in the streamwise direction as illustrated in Fig. 6. Fig. 7 presents normalised probability distribution functions of bubble and droplet chord sizes. Each data point represents the probability of bubble/droplet chord length in 0.25 mm intervals, e.g., the probability of chord length from 3.0 to 3.25 mm is represented by the data point

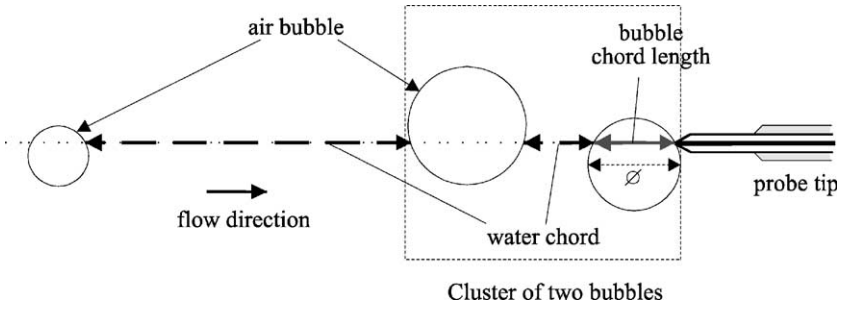

Fig. 6. Definition sketch of bubble and droplet chord length measurements.

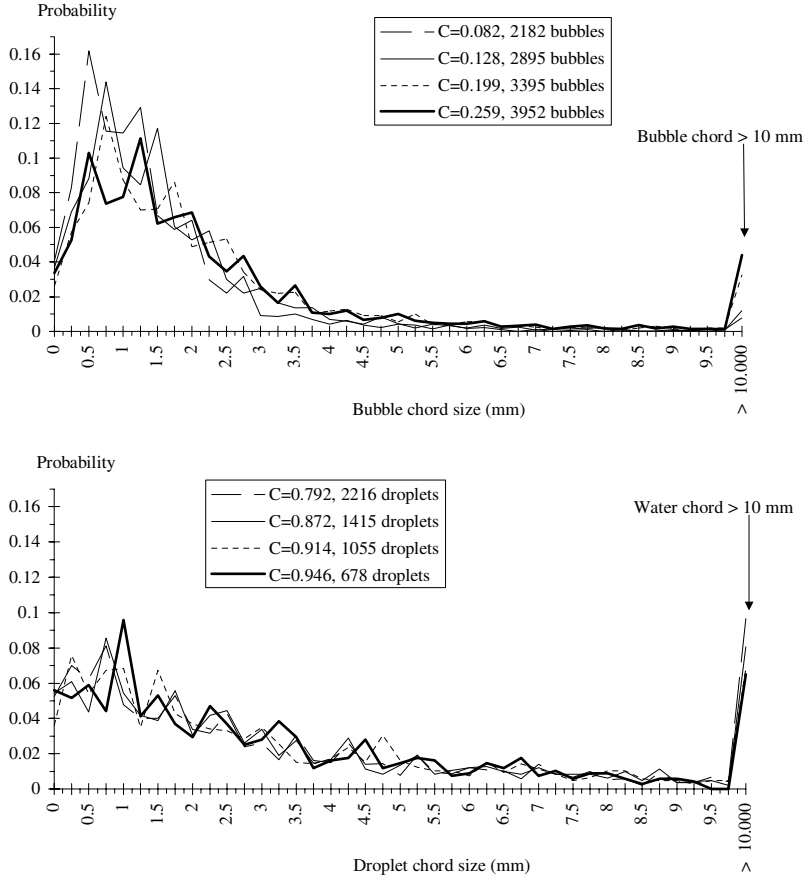

Fig. 7. Air and water chord length distributions in transition flow: $q_w = 0.0686$ m^2/s, $\alpha = 15.9°$, last step edge. Top: air chord lengths in the bubbly flow region ($C < 0.3$). Bottom: water chord lengths in the spray region ($C > 0.7$).

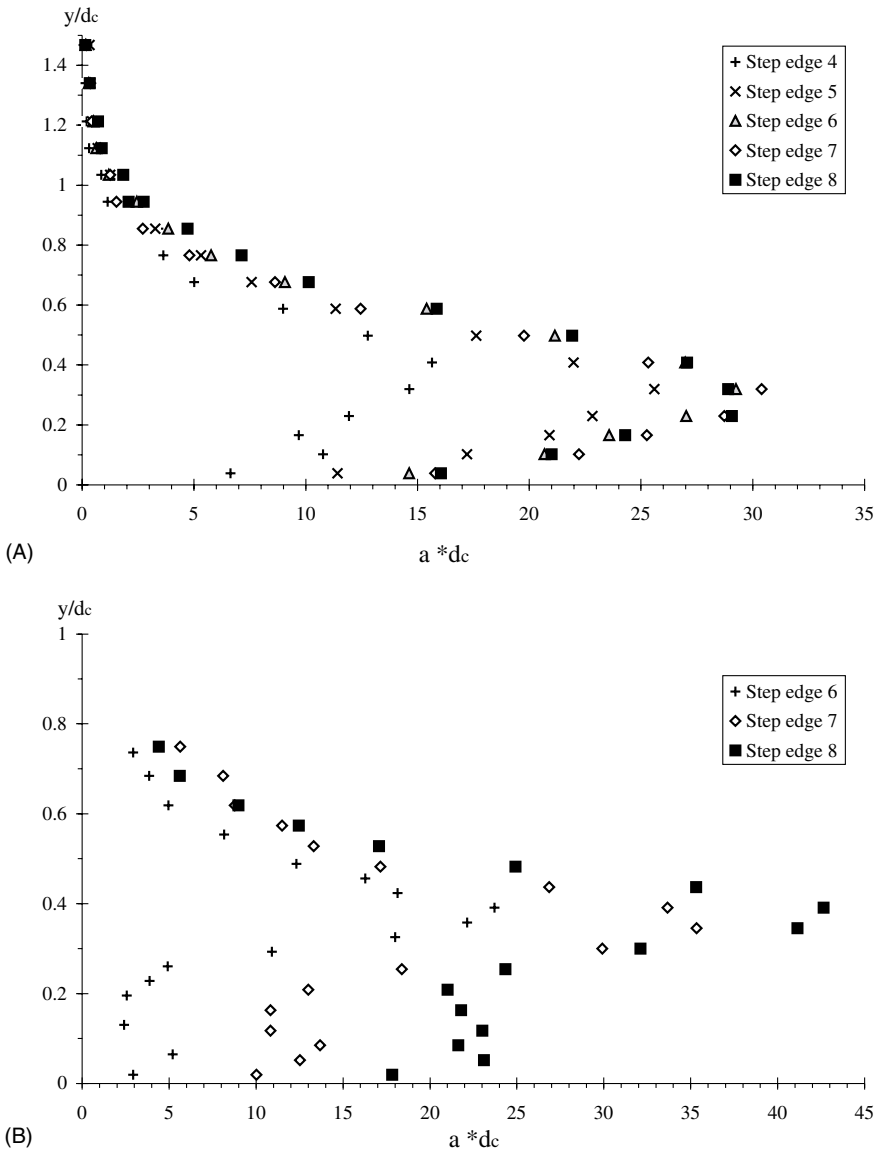

Fig. 8. Dimensionless distributions of air–water specific interface area: (A) transition flow, $q_w = 0.0686$ m^2/s, $\alpha = 15.9°$; (B) skimming flow, $q_w = 0.188$ m^2/s, $\alpha = 15.9°$.

labelled 3.0. The last column indicates the probability of chord lengths larger than 10 mm.

The results (Fig. 7) highlight a wide range of bubble and droplet chord lengths at each measurement location $\{x, y\}$. The chord length distributions are skewed with a preponderance of small chord sizes relative to the mean. The probability of air bubble chord lengths is the largest for bubble sizes between 0 and 2.5 mm in the bubbly flow region (Fig. 7 Top). It is worth noting the amount of bubbles larger than 10 mm. In the spray region ($C > 0.7$) (Fig. 7 Bottom), water droplet chord distributions present flatter, broader distributions than bubble chord distributions in the bubbly flow region ($C < 0.3$) (Fig. 7 Top).

4.2. Air–water specific interface area

The air–water specific interface area was estimated at each measurement point based upon particle size and void fraction measurements. Typical experimental data are presented in Fig. 8 for one flow rate. The results illustrate large air–water specific interface areas. At the most downstream step edge (black squares), maxima are 370 and 280 m^{-1} respectively in Figs. 8A and B, while the depth-averaged specific interface area amean is 265 and 173 m^{-1} respectively, where a_{mean} is defined as

$$a_{mean} = \frac{1}{Y_{90}} * \int_{y=0}^{y=Y_{90}} a * dy \quad (7)$$

Longitudinal distributions of the depth-averaged specific interface area show further a monotonic increase with distance. The result suggests an increasing number of entrained particles (bubbles and droplets) with distance in the flow direction, hence strong interactions between turbulence and entrained particles. The result indicates also that uniform equilibrium conditions in terms of interfacial properties were not achieved at the downstream end of the chute.

5. Turbulent velocity field

Two-phase flow velocity distributions are presented in Fig. 9 in terms of the time-averaged air–water velocity V and turbulence intensity $\mathrm{Tu} = u'/V$. The air–water velocity was calculated based upon a cross-correlation technique, and the turbulence intensity was deduced from the width of the cross-correlation function. Details of the processing technique were given in [6]. Fig. 9 includes transition and skimming flow data for the same flow conditions as in Fig. 4. In skimming flows, the velocity data compare favourably with a power law (Fig. 9 Bottom). The distributions of turbulence intensity Tu' exhibit relatively high turbulence levels across the entire air–water flow mixture (i.e. $0 \leqslant y \leqslant Y_{90}$) (Fig. 9). The trend, observed in both skimming and transition flows, differs significantly from well-known turbulence intensity profiles observed in turbulent boundary layers (e.g. [17]).

In clear-water skimming flows, a same shape of turbulence intensity profile was observed by Ohtsu and

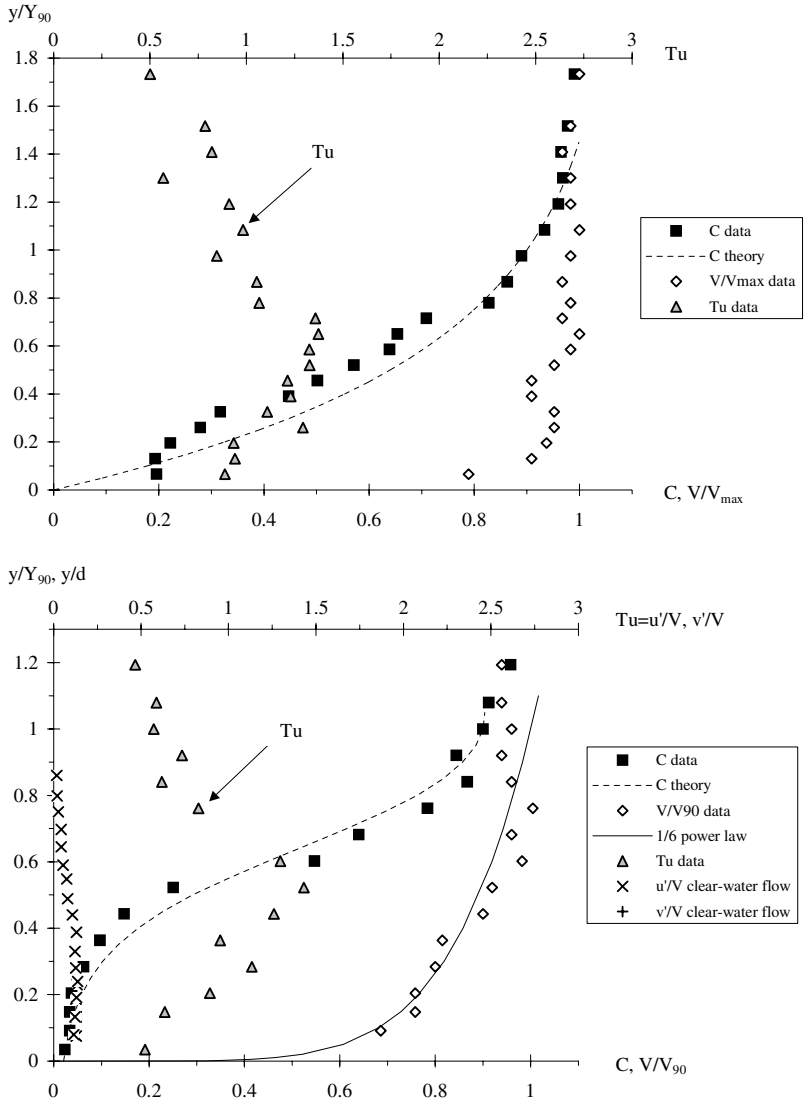

Fig. 9. Dimensionless velocity and turbulent intensity distributions. Top: transition flow $q_w = 0.058$ m^2/s, $V_{max} = 2.59$ m/s, $\alpha = 21.8°$, step edge 8. Bottom: skimming flow $q_w = 0.182$ m^2/s, $V_{90} = 3.47$ m/s, $\alpha = 21.8°$, step edge 8. Comparison with clear-water flow data $q_w = 0.089$ m^2/s, $\alpha = 19°$, $h = 0.05$ m [14].

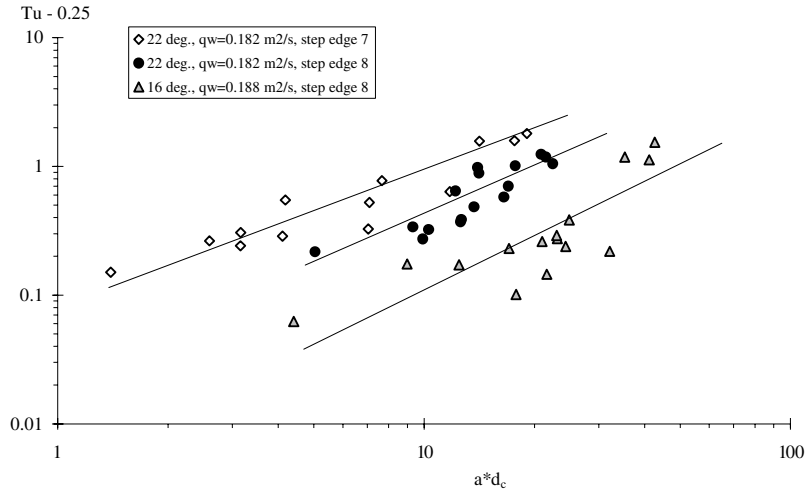

Fig. 10. Dimensionless relationship between specific interface area and turbulent intensity in skimming flow.

Yasuda [14]. These LDA measurements are shown in Fig. 9 Bottom, in terms of $\mathrm{Tu} = u'/V$ and v'/V, where u' is the root mean square of longitudinal component of turbulent velocity and v' is the root mean square of lateral component of turbulent velocity. Although the present quantitative values of turbulence intensity ($\sim$100%) are large, these are of the same order of magnitude as in wake flows between rocks [18], separated flows past cavities [9], and plunging jet flows [4].

In skimming flow, turbulence levels were markedly higher than monophase flow data for $0.1 < C < 0.9$, while they tended to observed clear-water turbulence intensities [14] of about 20–25% for $C < 0.1$ and $C > 0.9$. Fig. 10 presents the dimensionless relationship between specific interface area and turbulence intensity. Importantly the result shows a monotonic increase in turbulence intensity with increasing interfacial area. Fig. 10 suggests a strong correlation between turbulence level and air–water surface area. For a limited data set, the trend suggests that

$$\mathrm{Tu} - 0.25 \propto (a * d_c)^n \quad (8)$$

where the exponent ranges from about 1 to 3, depending upon the flow regime, discharge and step edge position.

6. Discussion

In open channel flows above a staircase invert, high turbulence levels are generated by the stepped geometry (Figs. 1 and 3). In turn, free-surface aeration is caused by turbulence fluctuations acting next to the air–water free-surface. Through this interface, air is continuously trapped and released. Interfacial aeration involves both entrainment of air bubbles and formation of water droplets (Fig. 2). The exact location of the interface becomes undetermined, and the "free-surface" or air–water interface area becomes the cumulative surface area of all air–water particles. During the present study, very large specific interface area were recorded (Fig. 8). In contrast, the depth-averaged specific area of clear-water open channel flow is $a = d^{-1}$ where d is the depth. Experimental results illustrates that the depth-averaged specific interface area in air–water flows is typically 1000 times greater than that in clear-water flow, for the present study (Fig. 8). As a result, the rate of mass transfer (Eq. (1)) is enhanced by a factor 1000 and possibly more because the residence time is enhanced by step form drag [3].

The writers hypothesise that large specific interface areas, associated with large number of particles and interfaces, contribute to an increase in turbulence levels. This is illustrated in Fig. 9, by comparing clear-water flow data with the present data in skimming flow, and by the strong correlation between turbulence levels and specific interface area shown in Fig. 10. For void fractions C and liquid fractions $(1 - C)$ greater than 5–10%, the air–water flow structure is dominated by collisions between particles (bubbles, droplets), and interactions between particles and turbulence. Such dynamic processes lead to continuous breakup, coalescence and interfacial deformations, which in turn generate large fluctuations in air–water interfacial velocity.

7. Summary and conclusion

Detailed air–water flow measurements were conducted down a stepped cascade. The study demonstrates the strong aeration (Figs. 1–5, 7 and 8) generated by high turbulence levels extending from the stepped invert up to the pseudo free-surface (Fig. 9). Air bubble and water droplet measurements highlight the broad spectrum of detected bubble/droplet sizes extending from

less than 0.25 to over 10 mm (Fig. 7). The air–water flow structure is associated with very large interfacial areas (Fig. 8).

Overall the large numbers of entrained bubbles/droplets contribute to substantial air–water mass transfer of atmospheric gases, and are correlated with high turbulence levels. The results explain the re-oxygenation potential of stepped cascades, used for in-stream re-aeration and in treatment plants.

Acknowledgement

The first writer acknowledges the helpful comments of Dr. Y. Yasuda (Nihon University, Japan).

References

[1] H. Chanson, Air Bubble Entrainment in Free-Surface Turbulent Shear Flows, Academic Press, London, UK, 1997.
[2] H. Chanson, in: The Hydraulics of Open Channel Flows: An Introduction, Butterworths–Heinemann, Oxford, UK, 1999, p. 512.
[3] H. Chanson, The Hydraulics of Stepped Chutes and Spillways, Balkema, Lisse, The Netherlands, 2001.
[4] H. Chanson, T. Brattberg, Air entrainment by two-dimensional plunging jets: the impingement region and the very-near flow field, in: Proc. 1998 ASME Fluids Eng. Conf., FEDSM'98, Washington, DC, USA, Paper FEDSM98-4806, 1998, p. 8 (CD-ROM).
[5] H. Chanson, L. Toombes, Stream reaeration in nonuniform flow: macroroughness enhancement, J. Hyd. Eng. ASCE 126 (3) (2000) 222–224.
[6] H. Chanson, L. Toombes, Experimental investigations of air entrainment in transition and skimming flows down a stepped chute, Application to Embankment Overflow Stepped Spillways, Research Report No. CE158, Department of Civil Engineering, University of Queensland, Brisbane, Australia, 2001.
[7] H. Chanson, Y. Yasuda, I. Ohtsu, Flow resistance in skimming flow: a critical review, in: H.E. Minor, W.H. Hager (Eds.), International Workshop on Hydraulics of Stepped Spillways, Zürich, Switzerland, 2001, Balkema, pp. 95–102.
[8] J.S. Gulliver, Introduction to air–water mass transfer, in: S.C. Wilhelms, J.S. Gulliver (Eds.), Proceedings of the 2nd International Symposium on Gas Transfer at Water Surfaces, Air–Water Mass Transfer, Minneapolis, MN, USA, 1990, ASCE, pp. 1–7.
[9] H.L. Haugen, A.M. Dhanak, Momentum transfer in turbulent separated flow past a rectangular cavity, J. Appl. Mech. Trans. ASME (1966) 464–641.
[10] F.M. Henderson, Open Channel Flow, MacMillan, New York, USA, 1966.
[11] Y. Kawase, M. Moo-Young, Correlations for liquid-phase mass transfer coefficients in bubble column reactors with Newtonian and non-Newtonian fluids, Can. J. Chem. Eng. 70 (1992) 48–54.
[12] Metcalf, Eddy, Wastewater Engineering. Treatment, Disposal and Reuse, third ed., McGraw-Hill, New York, 1991.
[13] D.B. Moog, G.H. Jirka, Stream reaeration in nonuniform flow: macroroughness enhancement, J. Hyd. Eng. ASCE 125 (1) (1999) 11–16.
[14] I. Ohtsu, Y. Yasuda, Characteristics of flow conditions on stepped channels, in: Proceedings of the 27th IAHR Biennal Congress, San Francisco, USA, 1997, Theme D, pp. 583–588.
[15] N. Rajaratnam, Skimming flow in stepped spillways, J. Hyd. Eng. ASCE 116 (4) (1990) 587–591.
[16] R. Robison, Chicago's waterfalls, Civil Eng. ASCE 64 (7) (1994) 36–39.
[17] H. Schlichting, Boundary Layer Theory, seventh ed., McGraw-Hill, New York, USA, 1979.
[18] B.M. Sumer, S. Cokgor, J. Fredsoe, Suction removal of sediment from between armor blocks, J. Hyd. Eng. ASCE 127 (4) (2001) 293–306.
[19] K. Toda, K. Inoue, Advection and diffusion properties of air bubbles in open channel flow, in: F.M. Holly Jr., A. Alsaffar (Eds.), Proceedings of the 27th IAHR Congress, San Francisco, USA, 1997, Theme B, vol. 1, pp. 76–81.
[20] L. Toombes, Experimental study of air–water flow properties on low-gradient stepped cascades, Ph.D. thesis, Department of Civil Engineering, University of Queensland, Brisbane, Australia, 2002.
[21] L. Toombes, H. Chanson, Air–water flow and gas transfer at aeration cascades: a comparative study of smooth and stepped chutes, in: H.E. Minor, W.H. Hager (Eds.), International Workshop on Hydraulics of Stepped Spillways, Zürich, Switzerland, 2000, Balkema, pp. 77–84.
[22] I.R. Wood, Air entrainment in free-surface flows, IAHR Hydraulic Structures Design Manual No. 4, Hydraulic Design Considerations, Balkema, Rotterdam, The Netherlands, 1991.